

Convolutional Neural Networks for Searching Superflares from Pixel-level Data of *TESS*

ZUO-LIN TU,¹ QIN WU,¹ WENBO WANG,¹ G. Q. ZHANG,¹ ZI-KE LIU,¹ AND F. Y. WANG^{1,2}

¹*School of Astronomy and Space Science, Nanjing University, Nanjing 210093, China*

²*Key Laboratory of Modern Astronomy and Astrophysics (Nanjing University), Ministry of Education, Nanjing 210093, China*

ABSTRACT

In this work, six convolutional neural networks (CNNs) have been trained based on 15,638 superflare candidates on solar-type stars, which are collected from the three-years observations of Transiting Exoplanet Survey Satellite (*TESS*). These networks are used to replace the artificially visual inspection, which was a direct way to search for superflares, and exclude false positive events in recent years. Unlike other methods, which only used stellar light curves to search superflare signals, we try to identify superflares through *TESS* pixel-level data with lower risks of mixing false positive events, and give more reliable identification results for statistical analysis. The evaluated accuracy of each network is around 95.57%. After applying ensemble learning to these networks, stacking method promotes accuracy to 97.62% with 100% classification rate, and voting method promotes accuracy to 99.42% with relatively lower classification rate at 92.19%. We find that superflare candidates with short duration and low peak amplitude have lower identification precision, as their superflare-features are hard to be identified. The database including 71,732 solar-type stars and 15,638 superflare candidates from *TESS* with corresponding feature images and arrays, and trained CNNs in this work are public available.

1. INTRODUCTION

The era of space time-domain astronomy is carrying huge chunks of observation data pouncing astronomy community. Astronomers have applied data mining methods including machine learning for processing observation data or revealing unforeseen statistical researches. For example, the convolutional neural network (CNN) was used to search strong lensing systems (He et al. 2020). Machine learning and recurrent neural networks (RNN) were used for detecting exoplanet transits (e.g. Rao et al. 2021; Cui et al. 2022; Ofman et al. 2022). Zhang et al. (2021) used random forest for classification of 4XMM-DR9 sources. Georgoulis et al. (2021) used deep learning methods for solar flare forecasting. Unsupervised clustering method was used for classifying fast radio bursts (FRBs) (Chen et al. 2022). CNNs were used for searching FRBs from radio data (e.g. Agarwal et al. 2020; Yang et al. 2021), etc.

Superflares are stellar bursting phenomena with duration and energy larger than typical solar flares (Hudson 2021). They have severe impacts on the space weather around the star and exoplanets (e.g. Segura et al. 2010; Airapetian et al. 2016; Lingam & Loeb 2017; Atri 2017). Many works have used *Kepler* data to build the connection between solar flares and stellar superflares (Maehara et al. 2012; Shibayama et al. 2013; Maehara et al. 2015; Notsu et al. 2019). Tu et al. (2020, 2021) used *TESS* data and LAMOST spectroscopic data to strengthen the view that superflares can be generated by isolated stars (e.g. Shibata et al. 2013), instead of through star-planet interactions (e.g. Rubenstein & Schaefer 2000; Ip et al. 2004). Doyle et al. (2020) found no preference for the rotational phase of superflares. So, stellar activities including superflares become a vital topic as the Sun can also generate superflares itself but with much lower possibility. Even that, one superflare from the Sun will of cause risk habitability of the Earth.

With the limitation of observational techniques, detailed observations of distant stars seem impossible. Superflares on other stars may give us a chance to statistically study stellar activities. The most crucial step is collecting enough true superflare events. From Maehara et al. (2012) to Tu et al. (2021), superflare candidates are selected through automatic algorithm and then visually inspect them. Honestly, it takes too much time to verify true superflare events.

However, this also enhances our experiences of visual inspection. Actually, back to 2018, [Vida & Roettenbacher \(2018\)](#) used random sample consensus (a traditional data mining method) to find flares in *Kepler* data. [Feinstein et al. \(2020\)](#) used CNN to search stellar flares in *TESS*, and their network was used in subsequent research ([Feinstein et al. 2021](#)). [Vida et al. \(2021\)](#) used RNN to search stellar flares in *Kepler* and *TESS* data.

Above works including CNN and RNN methods enhance the efficiency and automatization for searching stellar flares. And these methods surely improve the accuracy of those collected superflares than other traditional light-curve outliers searching algorithm like fitting the quiescent variability (e.g. [Walkowicz et al. 2011](#); [Wu et al. 2015](#); [He et al. 2018](#)), iterative σ -clipping approach (e.g. [Yang & Liu 2019](#)), etc. However, according to these papers ([Vida & Roettenbacher 2018](#); [Feinstein et al. 2020](#); [Vida et al. 2021](#)), they all just used stellar light curves to search for stellar flare events. According to our experience on visual inspection of superflare candidates from pixel-level data, there are a number of candidates showing superflare features on light curves, but without any superflare signals from pixel-level data. Obviously, this kind of candidates should not be convincingly treated as superflare events. Their superflare-like shapes in stellar light curves may be caused by CCD noises, pipeline errors or other intrusive disturbing factors. Visual inspection of pixel-level data is the most direct way to exclude the contamination from false positive events. Naturally, we pursue a machine learning method basing on pixel-level data, which excludes as much false events as possible, instead of basing on stellar light curves only. Then, a database including true superflares can be constructed by machine learning methods. Basing on this database, statistical study of stellar activities is more reliable and scientifically valuable. So, in this work, we attempt to use the deep learning methods such as CNN, and ensemble learning methods including stacking and voting, to search for superflare events from pixel-level data of *TESS*. We expect that CNNs can more accurately search true superflare events basing on pixel-level data.

This paper is organized as follows. In Section 2, we briefly articulate the process of selecting solar-type stars and superflare candidates. All candidates through our improved data pipeline have been visually inspected and classified into three classes. In Section 3, the construction of data sets and structured six CNNs according to six feature data are given. Ensemble learning including stacking CNN and voting are also performed in Section 4. Results of CNNs, comparing CNNs and some discussions are given in Section 5. Summary is presented in Section 6.

2. SOLAR-TYPE STARS AND SUPERFLARE CANDIDATES

In this section, we will briefly illustrate how to select solar-type stars and search superflare candidates for training CNNs. For more details, one could refer to our previous works ([Tu et al. 2021, 2020](#)). Differences and improvements will be specifically discussed in the following.

2.1. Selection of solar-type stars

We select solar-type stars according to following criteria: (1) stellar effective temperature (T_{eff}), $5100\text{K} \leq T_{\text{eff}} < 6000\text{K}$, and (2) surface gravity ($\log g$), $\log g > 4.0$ (e.g. [Shibayama et al. 2013](#); [Maehara et al. 2015](#); [Tu et al. 2020, 2021](#)). $\log g$ and T_{eff} are both gathered from *TESS* input catalogue (TIC v8) ([Stassun et al. 2019](#)). *Hipparocos-2* catalog ([van Leeuwen 2007](#)) and *Gaia*-EDR3 (*Gaia* early data release 3; [Gaia Collaboration et al. \(2020\)](#)) are used to mark those solar-type stars which are possible binary systems or contaminated by brighter stars within $21''$ distance. *Gaia*-EDR3 gives T_{eff} estimations, with some from *Gaia*-DR2 ([Gaia Collaboration et al. 2018](#)).

Specifically, from all 71,732 solar-type stars, 277 stars are possible binary systems according to *Hipparocos-2* catalog. After cross-matching with *Gaia*-EDR3 catalog, 753 stars are with brighter stars in less than $21''$ distance which can not be distinguished by *TESS*. 739 stars are with brighter stars in the distance greater than $21''$ and less than $42''$. Unlike what we did in the work before ([Tu et al. 2021](#)), instead of excluding those stars which are binary systems or contaminated by brighter stars, we flag these stars in our database. Because, instead of judging whether superflares are purely from solar-type stars, this work focus on selecting superflare candidates according to their light curves with superflare-shapes or features. So, we keep those stars with unique flags without excluding them. This will also enhance the purpose of collecting as much data as possible in order to obtain better performance of CNNs. Besides, 5,435 stars may contain M-dwarf candidates within $42''$ range. As *Gaia*-EDR3 do not include $\log g$, and Section 3.1 of [Tu et al. \(2021\)](#) demonstrated that observations of solar-type stars may not be influenced by M-dwarf stars, these stars are not excluded but marked with flags. Totally, 71,732 solar-type stars from three-years observation of *TESS* are collected.

We use pre-search data conditioned (PDC) light curve of every single star for period estimation and photometric variability calculation. Periods of these stars are estimated through the Lomb-Scargle method ([Lomb 1976](#); [Scargle 1982](#)). We also set the false alarm probability as 10^{-4} to estimate periodicity of a star (e.g. [Cui et al. 2019](#)). Photometric

variability (R_{var}) is derived by

$$R_{\text{var}} = F_{95\%} - F_{5\%}, \quad (1)$$

where $F_{95\%}$ and $F_{5\%}$ stand for the upper 95% and lower 5% of ranked normalized flux of stellar light curves (Basri et al. 2010). The first- and third-year observations of *TESS* both cover the southern hemisphere of the sky. Stars in this area are observed multiple times, so their period and R_{var} are calculated basing on all observations from *TESS*. Specific information of 71,732 solar-type stars can be found in Table 1.

2.2. Superflare candidates

Basically, we select superflare candidates through the same method as in Tu et al. (2020, 2021). Each solar-type star's PDC light curve from *TESS* has been checked by the automatic algorithm. The updated algorithm has been used to process *TESS* second-year observation (Tu et al. 2021). Briefly, those outliers in the light curve are selected by the following equation,

$$\Delta F^2(t_{i,n}) = s(F_i - F_{i-n-1})(F_{i+1} - F_{i-n}), \quad (2)$$

where F is the normalized flux of one sector. And $s = 1$, when $(F_i - F_{i-n-1}) > 0$ and $(F_{i+1} - F_{i-n}) > 0$ are both satisfied, otherwise $s = -1$. We set $n = 5$ and $n = 2$ to search outliers twice, as n describes the rising time of flares (Tu et al. 2020). If $n = 2$, we cut 0.05 days before, and 0.10 days after the peak flux as flare light curve interval for further analysis. Correspondingly, if $n = 5$, we use 0.15 days before, and 0.25 days after the peak flux. Stellar luminosity is calculated through Stefan-Boltzmann law

$$L_* = 4\pi R_*^2 \sigma_{\text{sb}} T_{\text{eff}}^4, \quad (3)$$

where stellar radius R_* and surface temperature T_{eff} are taken from TIC v8 catalog. In order to get the start and end times of a flare, the beginning 26.7% together with the ending 33.3% of the flare light curve are fitted by quadratic function $F_q(t)$. And we can get

$$F_{\text{flare}}(t) = F(t) - F_q(t). \quad (4)$$

The first and lost points, whose photometric errors $F_{\text{error}}(t)$ satisfied the following equation, are set to be the start and end time of a flare,

$$3 \times F_{\text{error}}(t) < F_{\text{flare}}(t). \quad (5)$$

$F_{\text{flare}}(t_{\text{peak}})$ at peak point stands for the peak amplitude of a flare. We estimate superflare energy by the equation

$$E_{\text{flare}} = \int L_* F_{\text{flare}}(t) dt, \quad (6)$$

where stellar luminosity, flare flux are calculated in Equations (3) and (4), and the integral is from the start to the end time of a flare. Totally, 15,638 flare candidates are selected from all solar-type stars in the three-years observations of *TESS*.

We classify all candidates into three classes, through visual inspection of their pixel-level information according to the images shown in Figure 1. These three classes are Gold-class, Silver-class and None-class.

- Gold-class collects those candidates which show standard superflare features with rapid rising and slow decaying shapes in light curve. From pixel-level information, superflare signals show shapes of a standard point spread function (PSF) as shown in the panel (e) and (f) of Figure 1, where flare signals close to stellar center pixel are obviously stronger than other pixels nearby. And almost all pixels in the *TESS* aperture show superflare signals as shown by the panel with un-normalized flux. Patterns in Row 2 of Figure 2 are same with those in Figure 1, from which this candidate is convincingly classified as Gold-class.
- Silver-class gathers superflare candidates which do not perfectly show flare features unlike those in Gold-class do. Data of Silver-class may also show flare signals from pixel-level data of normalized flux, but with a little bit higher noise around. Pinnacle-shape light curves can be also seen from the panel with un-normalized flux. An example is shown in the Row 1 of Figure 2.
- None-class collects other candidates, which are false events including planets transit, and cosmic ray signals etc. Row 3 of Figure 2 gives an example of None-class. We hardly find pinnacle-shape light curves in pixel-level data. Even if a few light curves with un-normalized fluxes show a pinch of flare-shape features, unrelated noise are strongly dominant.

To be clear, the candidates in the Gold-class and Silver-class are all true superflares. The reason to split these superflares into two categories is that the Silver-class has its own features which are different from those of Gold-class. In order to improve the performance of CNNs, we should separate them.

All 15,638 candidates are classified into these three categories by visual inspection at least three times by our groups. Detail information can be found in Table 2. For the convenience of users who are only interested in data of superflares, the duration, peak luminosity and energy of superflares are collected in this table. These information will be concealed for those candidates if at least one of following criteria is satisfied. (1) The hosting stars are with flags HB or GB21 in Table 1 after cross-matching with *Hipparocos-2* and *Gaia*-EDR3 catalogs. (2) Candidates' rising epoch is longer than decaying epoch. (3) Candidates are visually inspected and classified as None-class. A column in Table 2 list all file names which corresponding to feature images and arrays used for CNNs' training, and will be articulated in Section 3.1.

3. DEEP LEARNING

This section will articulate the process to get three dimensional arrays and feature pictures for training CNNs, and how we set training, validation and test data sets. Specific structures of six networks are also shown. Two methods of ensemble learning are used for enhance performances of CNNs, including stacking and voting.

3.1. Three dimensional arrays and feature images

This work focus on auto-identification of superflares through pixel-level data of *TESS*. Figure 1 and Figure 2 reveal pixel-level light-curves, according to which we visually classified those superflare candidates into three classes.

Specifically, we transform pixel-level data into arrays and feature images for further CNNs' training. The first data format is three dimensional array as visualized in Figure 3(a). One dimension of this data is time, and the other two are pixel indexes. This array contains original pixel-level information during the whole flare light curve interval. One may comprehend these arrays as short film clips which record changing of pixel-level image in just 0.15 days. The image from *TESS* data contains 11×11 pixels, and with 2-minutes cadence. So, these three dimensional arrays are with the size of $11 \times 11 \times 108$. These arrays contain original observations of flare candidates from *TESS*.

Then, we transform the array into pixel-level light curves as shown by Figure 3(b), which is exactly the same as that shown in the panel (e) and (f) of Figure 1. In this feature picture, we list 11×11 squares which correspond to 11×11 pixels of *TESS* pixel-image data. By this procedure, we reduce three dimensional data into two-dimension images. In each square, light curve of the corresponding pixel is revealed in Figure 3(c). In order to reduce complexities of the following CNNs, we set the peak time of each pixel-level light curve at the 1/3 position of the time axis. Besides, the blue frames stand for those aperture masked by *TESS* pipeline. In order to reduce the color information which is totally unrelated with superflare searching, the feature image is transformed to gray-scale image with just one channel (traditional colorful images are with RGB three-channels), as shown in Figure 3(d). In order to protrude the pinnacle-shape of superflare light curves, the areas under the light curves are filled. We use white color for those light curves which are from those aperture pixels masked by *TESS*, so they are distinguished from other ordinary light curves which are in grey.

Further, we line-up sequences of all 11×11 pixel light curves, and reveal the flux by gray-scale color as shown in Figure 3(e). Each line of this feature image stands for the corresponding pixel, and from left side to right side stands for time axis of flare light curve. For example, in the image, the line of pixel No. 60 suddenly brighten and gradually darken, which means the rapid rising and slowly decaying of the light curve.

As unnormalized and normalized fluxes are both derived, we have two versions for three-dimension arrays, images of pixel-level and line-up sequences of light curves. These six kinds of data are visualized in Figure 4. Then we construct six CNNs for all of them. All of these six feature images and arrays are from a superflare candidate. In other words, we intend to use the six CNNs to classify just one superflare candidate, because these feature images and arrays describe a candidate from different angles even according to the same pixel-level information from *TESS*.

- Three-dimension arrays (TD-arrays) are basically original records of *TESS* observations but without any details of *TESS* aperture masks.
- Pixel-level images (PL-images) are with information of *TESS* aperture masks, and show pixel-level PSF shape of a true superflare, which shows relationships between stellar center pixel and nearby pixels.

- Images of line-up sequences light curves (LS-images) more obviously reveal contrast of dark and bright, which more delicately portray the rapid rising and slow decaying phases of superflare light curves. However, LS-images deficient in any information of *TESS* aperture masks.

3.2. Training, validation and test data sets

As we introduced in Section 2.2, 15,638 flare candidates are selected and classified into three classes including 1,268 data in Gold-class, 3,792 data in Silver-class and 10,578 data in None-class data. For convenience of the further k-fold cross validation of CNNs, we randomly split 15,638 candidates into seven stacks. Figure 5 shows the work flow of this process. Each of the six stacks contains 2,348 data, and the last stack contains 1,550 data. Basically, the test set takes 15% of whole data set. From these stacks, we choose each of them as test data set, and others are integrated and then evenly split into ten mini-stacks. One of mini-stacks is set as validation data set, the others are combined as training data set. Validation set takes about 10% of the whole database, and training set takes 75%. According to above flows, one test data set corresponds to ten validation and ten training data sets. As there are no intersection data among test, validation and training data sets, we obtain 70 clusters of data (7 test sets \times 10 training and validation sets). Each one includes a training set, a validation set and a test set. As these three classes are data imbalanced, above stacks and mini-stacks are artificially data-balanced and contain basically same proportions of three classes.

3.3. Convolutional neural networks

We have set the training, validation and test data sets, then we construct six CNNs according to candidates' TD-arrays, PL-images and LS-images. The validation data set is used for modulate hyper-parameters of networks. Before we select six CNNs for each of TD- PL- LS-normal. and unnormal. data, we should construct a whole bunch of networks, and select the most stable and outstanding one according to the validation data set.

Flow charts of these six CNNs are shown in Figure 6. We use AdaGrad algorithm (Duchi et al. 2011) as optimizer when training networks. Learning rate, learning rate decay and weight decay are all listed in the figure for each of these networks. None of these networks are same, as we consider different identities of feature images and arrays. Stability shown by validation data after applying for each network is also regarded. Note that, in order to standardize inputs of each network, we resize PL-images and LS-images with resolution of 704×704 and 121×121 , respectively. TD-arrays are all resized to $11 \times 11 \times 110$ through interpolation along time-axis. We use outputs which are applied Softmax function (normalized exponential function Bishop (2006)) as following

$$c_i = \frac{e^{o_i}}{\sum_{j=0}^K e^{o_j}} \quad \text{for } i = 0, \dots, K. \quad (7)$$

As we only have three classes, $K = 2$. o_i represents the original output for the i^{th} class. So, after exponentially normalized, c_i represents the possibility for classifying one input candidate to i^{th} class. We choose the maximum number of c_i to classify the input into i^{th} class. During training networks, cross-entropy loss function is used, which can be derived as

$$\ell = -\frac{1}{n} \sum_{j=1}^n \sum_{i=0}^K t_i^{(j)} \log o_i^{(j)}, \quad (8)$$

where $K = 2$ and n stands for the number of class and counts of data in the training set, respectively. j means the j^{th} data of training set. $t_i = 1$ if the j^{th} data is artificially classified into the i^{th} class, otherwise $t_i = 0$. The purpose of training networks is to reduce value of loss function and raise accuracy of classification. Besides, as the three classes are data imbalanced, data re-balance is also realized through cross-entropy loss function by multiplying proportions of these three classes in training set.

Results of 70 training and validation data sets are shown in Figure 7. These can be also treated as results of k-folding cross validation. Note that, we classify candidates into three classes, however both Gold-class and Silver-class contain superflare events. So, results from these two classes are combined to calculate accuracy of a network. The reason why we set three classes has been illustrated in Section 2.2. From the figure, we can see that the loss and accuracy of six networks are more stabilized as training epochs increasing. Some of networks show a little bit over-fitting that the accuracy of validation is relatively lower than the training set. This is caused by two reasons. First, we only have about 15,000 data, and the networks may relatively complicated with much neural units which should be well constrained by even more data. Second, we tend to choose those networks which perform well on validation data with results of

higher accuracy and stable training progress. We have also tried to simplify those networks or put penalty on loss function with higher weight decay. However, none of these will enhance the performance of networks, but reduce it. So, we control over-fitting by adding dropout layers in between convolutional layers, and setting learning rate decay to avoid relatively higher learning rate as learning epochs increase.

		CNN results	
		Positive	Negative
Real truth	Positive	TP	FN
	Negative	FP	TN

(9)

In the matrix (9), we list an example of the confusion matrix which is helpful when we introduce recall, precision, true positive rate (TPR) and false positive rate (FPR). In this matrix, TP , FN , FP , and TN stand for numbers of true positive, false negative, false positive and true negative events. In this work, true events are superflare events. The real truth is artificial classification. CNN results are classifications based on CNNs' outputs. So, accuracy, recall (R), precision(P), TPR and FPR can be derived as

$$\text{Accu.} = \frac{TP + TN}{TP + FN + FP + TN}, \quad (10)$$

$$R = TPR = \frac{TP}{TP + FN}, \quad (11)$$

$$P = \frac{TP}{TP + FP}, \quad (12)$$

$$FPR = \frac{FP}{FP + TN}. \quad (13)$$

Break-Even Point (BEP) and Area Under ROC (Receiver Operating Characteristic) Curve (AUC) are also derived from those networks' results. BEP are points where precision equals recall in the PR -curve, which are derived by setting limits at each of ranked possibilities of positive events to calculate specific recall and precision. ROC-curve is also setting these limits and calculate specific TPR and FPR . AUC is the area under this curve. The best network is with $\text{Accu.} = 100\%$, $R = TPR = 1$, $P = 1$ and $FPR = 0$, from $\text{BEP} = 1$ and $\text{AUC} = 1$, which means that the network can ideally recall all positive events with 100% precision, and perfectly distinguish positive events from negative events.

Each of the seven test data sets is inputted into corresponding networks. For example, the test set in Figure 5 is stack-0, which is inputted into networks trained by using data from combination of mini-stacks without mini-stack-0. Then, the same test set is inputted into networks trained by data without mini-stack-1, and so on. This test set is inputted into corresponding networks ten times, so do other test sets. Finally, we get 70 results for each of six networks. Their accuracy, recall, and precision are all listed in Table 3. As these results are from test data set, these properties can indicate generalization ability of CNN. These results are based on classification of superflares or non-superflares instead of three classes as we illustrated above.

4. ENSEMBLE LEARNING

Six CNNs for TD-arrays, PL-images, and LS-images do not show perfect performance with even higher accuracy. So, we try to find a way to improve accuracy for classifying superflare candidates. After training six separate networks, ensemble learning is a handy way, including stacking and voting methods etc. Here, we illustrate these two methods, through which we improve the superflare classifying accuracy.

4.1. Stacking

Stacking method can also be understood as training another CNN network (hereafter stacking-CNN), whose inputs are combination of those outputs from many individual networks (Wolpert 1992; Breiman 1996). As we introduced in Section 3.2, we have 7 test sets \times 10 training and validation sets. And each test set, validation set and training set are independent. For one test set, there are ten training and validation sets. In order to avoid over-fitting of training stacking-CNN, outputs of inputting training data set into trained networks (six CNNs) are not used for training

stacking-CNN (Zhou 2021). These six networks are illustrated in Section 3.3. For instance, stack-0 in Figure 5 is treated as a test set. Firstly, we input the validation set mini-stack-0 and the test set into six networks, which are trained by using remaining mini-stacks, and we get the first 1/10 training data (train-part-0) and first test set (test-stack-0) for stacking-CNN. Then, we use the mini-stack-1 and the same test set into the networks, which are trained by the remaining mini-stacks, and get the second 1/10 training data (train-part-1) and second test set (test-stack-1), and so on. Finally, for the test set stack-0, we have ten test-stacks and one training data combined by the ten train-parts. There are seven test sets (a.k.a stacks in Figure 5). So we get seven corresponding training sets. Each one of them corresponds to ten test-stacks for stacking-CNN, respectively. The outputs of six networks are combined as an array with size of 6×3 (each of six networks outputs an array with size 1×3) and inputted into stacking-CNN. The new 7×10 test-stacks are used for k-folding cross validation of stacking CNN. Work flow of stacking-CNN can be found in Figure 8(a). Results of putting 70 test-stacks into trained stacking -CNN are listed in Table 3. These 70 test-stacks are also used in the following voting method.

4.2. Voting

Voting is another method to integrate many separate CNNs, whose outputs are treated as votes to classify the candidates. Here, we use two voting actions including soft-voting and hard-voting, which can be formulized as

$$S(x) = [s_i(x) \text{ for } i \in \{0, 1, 2\}], \quad (14)$$

$$\text{where } s_i(x) = \frac{\sum_{j=1}^6 c_i^j(x)}{\sum_{i=0}^2 \sum_{j=1}^6 c_i^j(x)}, \quad (15)$$

and

$$H(x) = [h_i(x)/3 \text{ for } i \in \{0, 1, 2\}], \quad (16)$$

$$\text{where } h_i(x) = \begin{cases} h_i(x) + 1 & (\arg \max \{c^j(x)\} = i \text{ for } j \in \{1, 2, 3, 4, 5, 6\}) \\ h_i(x) + 0 & (\arg \max \{c^j(x)\} \neq i \text{ for } j \in \{1, 2, 3, 4, 5, 6\}) \end{cases}. \quad (17)$$

Here, $S(x)$ and $H(x)$ stand for soft-voting and hard-voting, and x is the candidate data needed to be classified. c_i^j is output applied by Softmax function in Equation 7. i is the i^{th} class, as we classify candidates into three classes (Gold-class, Silver-class and None-class), $i \in \{0, 1, 2\}$. j is the j^{th} networks from 1 to 6. The corresponding orders of networks are listed as the first six rows of Table 3. Specific work flows of voting are shown in panel (b) and (c) of Figure 8. In order to strictly classify candidates through the voting method, we set a limit at 75%. So, $\max H(x)$ and $\max S(x)$ should be larger than this limit, then the candidate can be labeled. Otherwise, voting method refuses to label the candidate, and data is remained for artificial labeling after visual inspection. For hard-voting, 75% means more than four of six individual networks have same voting result. As some candidates are refused to be classified, we define the classification rate which can be derived as

$$\text{Class.rate} = \frac{N - N_{\text{TBD}}}{N}, \quad (18)$$

where N is data counts of all data of a test-stack, and N_{TBD} is the number of data, which are refused to be classified and labeled as ‘TBD’ in voting flows. As the outputs applied by Softmax function can be treated as possibilities for classifying candidate, we regard that each of the six CNNs has 100 votes. For soft-voting, 75% means that more than 75% of 600 votes support same voting result. We do not set this kind of limit for those six separated CNNs. The reasons are as follows. (1) There is no practical meaning for the limit, if we set it for each of six CNNs. (2) It is hard to get a specific percentile limit, which should be reasonable and explicable. (3) Even if we set 75% as limits for each of six CNNs, accuracy and other properties are not showing better results than voting methods. (4) Voting from the six CNNs can reject to classify those candidates which may be hard to be classified or CNNs are not trained with before. So, we insist to use the maximum outputs of each six CNNs to classify candidates instead of set a limit. The results of voting methods are listed in Table 3.

5. RESULTS AND DISCUSSIONS

5.1. *Public open data set*

In Section 2.2, we have introduced the method, through which we select superflare candidates from three-years observation of *TESS*. These superflare candidates are all from solar-type stars. These 15,638 candidates are listed in Table 2 and the corresponding stellar properties of target stars are listed in Table 1. Note that, although the stellar periods may be combined three-years observations, we should be careful when using the periods larger than 10 days. Because a sector of *TESS* is with a limited observing span of about 27 days, and the observation of each sector is normalized by itself (Tu et al. 2020). We classify these data into three classes: Gold-class, Silver-class, and None-class, among which Gold- and Silver-class all collect superflare events. As these three classes are with different specialties, and in order to improve the performance of CNNs, we still use three classes for training CNNs, but use superflare events or non-superflare events as a binary classification problem to calculate properties of CNN. Three classes with their own characters are articulated in Section 3.1 and shown in Figure 2.

We emphasize that these candidates are classified into three classes and visually inspected at least three times. However, we do not statistically use these data to do any research like Tu et al. (2020, 2021), which is beyond the topic of this article. For readers who are interested into these data, they can find corresponding events as specific information are all released. One could also use these data to get creative feature images or data for their own CNNs' training. Besides, the six kinds of data sets including TD-normal. TD-unnormal. PL-normal. PL-unnormal. LS-normal. and LS-unnormal. are all public released. Their corresponding file names are also listed in Table 2. So, these data sets are really useful and valuable for the community of searching for stellar superflares. They are useful for searching superflares on other types of stars, as deciding the type of a star is totally irrelevant with detecting superflare candidates, which is only according to light curve and pixel-level data.

5.2. *Comparing CNNs*

We compare results of these networks and methods listed in Section 3.2. These result are listed in Table 3. The classification rate, accuracy, recall, precision, BEP and AUC are used to indicate generalization capabilities of different CNNs and methods. Note that, (1) In order to compare results from those six different CNNs, we use same seven test sets (stacks in Figure 5). Each one of these six CNNs is trained once by each of ten training data sets, so we totally get 70 outputs (7×10). The only difference is the inputs of these CNNs, which are different corresponding feature images or arrays. For voting and stacking methods, 70 test-stacks in all are inputted into corresponding stacking-CNNs, which are trained by each of seven training sets. The processes of setting data sets for deep learning and ensemble learning are introduced in Section 3 and Section 4. So, the original candidates and counts of data in each of three classes are all the same when comparing these CNNs and voting methods. (2) The ultimate purpose of this work is to efficiently distinguish superflare events and non-superflare events. Although we set three classes to improve six CNNs' performance, the results according to two class classifications (superflare or non-superflare) are obtained. According to the results of the two-class classifications, we discuss using these CNNs to search superflares in the future.

For comparing these CNNs and voting methods, the properties in Table 3 are visualized in Figure 9. From this figure, the accuracy of these six CNNs is around 95.5%. It is obvious that TD-normal is the best network of these six CNNs and we use the properties of it to compare with stacking and soft-voting in Figure 10. As shaded area (std intervals) of the six CNNs is relatively larger than that of stacking and voting methods, the six CNNs may be not very stable than stacking CNN and voting methods according to all test sets. We also compare PR-curves and ROC-curves of the TD-normal. stacking CNN and soft-voting in Figure 10. Both of these two curves indicate generalization and performance of a CNN. Comparing with CNN of TD-normal., the accuracy and other properties of stacking CNN are significantly enhanced. The six CNNs and stacking CNN are both classifying all candidates with 100% classification rate, unlike voting methods. This notable enhancement strengthens the idea that each of six CNNs and inputs of them are totally with their own individuality. Combination of these six CNNs could improve redundancy or error-tolerant rate of searching superflares. From figure 10, it is noticeable that the performances of ensemble learning methods are more enhanced than six CNNs. Only through one CNN to get higher generalization performance is not that practical as we only use less than 15,368 data to train a network, and only about 1/3 of them are labeled superflare events. The well-known deep learning benchmark database like MINIST (Lecun et al. 1998; Kussul & Baidyk 2004) and Fashion-MNIST (Xiao et al. 2017) are with 60,000 training instances, even if they are classified into ten classes, and each class is definitive with clear boundaries. In this work, only superflare events are distinguished from other non-superflare events with clear features and boundaries. However, it is also possible to classify many sub-classes in

None-class like exoplanet transient, cosmic ray events, CCD errors, and pipeline noise etc. For convenience, we blend all these non-superflare events in the None-class to distinguish with superflare events, which may confuse CNNs when non-superflare events are inputted. So, limited instances of superflares and blending all non-superflare events together may be the reason why we do not get a single CNN which is better, more stable and comparable to ensemble learning methods yet. It is more complicated when we use ensemble learning methods, as we have to train and get six kinds of CNNs and input data, but ensemble learning is now a practical and relatively powerful method when we try to classify superflare candidates. Besides, the stacking CNN, hard-voting and soft-voting are more stable and better than six CNNs according to Figure 9.

If we describe the enhancement of stacking CNN as taking advantage of differences between six CNNs and their inputs, voting methods are more emphasized to use result consistency of these six CNNs. For voting methods, accuracy, recall, precision, BEP and AUC are calculated basing on those classified candidates apart from others labeled as ‘TBD’ after voting, as shown in Figure 8(b) and 8(c). Comparing the stacking CNN with voting methods in Figure 9, it is evident that voting methods are more stable and exceptional. And soft-voting performs better than hard-voting. In Figure 10, soft-voting is really close to the ideal vision of a classification machine learning method, whose $R \sim 1$, $P \sim 1$, $FPR \sim 0$ and $TPR \sim 1$. But classification rate decreases from 100% to about 92% as shown in Figure 9. This is a trade off between performance and classification rate of a CNN. Voting methods evenly consider each of six CNNs, through uniting outputs of these six CNNs. As we set 75% as a limit, over which a candidate is classified, this can be understood to ensure voting results are broad representative and accurate among these six CNNs. We also checked those candidates whose maximum voting results were not up to 75% limitation. These candidates are intractable even through visual inspection as their signal to noise ratios (SNR) are relative low and hard to be classified. This may be resulted from the reason that each of six CNNs is also hard to be trained to detect superflare features at such low SNRs. Another reason might be that some kinds of data have not been paid adequate attention to as their data are not enough in training sets. These kinds of data may not be well learned by CNNs, and rejected for classification. Voting method maximally exposes these unclassified data with about 8% exposure rate ($100\% - 92\%$) for soft-voting. Besides the descending of classification rate (derived in Equation 18), other indicators of networks’ generalization and performance are all enhanced distinctly as shown in Figure 9, and accuracy are improved even higher than 99%. So, we could improve the accuracy of soft-voting higher than 99.42% with hypothesis that the artificially visual inspection are 100% accurate and trustworthy. For the reason that some kinds of data are not enough to be paid adequate attention to while training CNNs, it is likely that some data may be new transient phenomena. Through one-on-one specifically visual inspection, we will find these new phenomena instead of submerging them into endless data. Back to our initial purpose of using CNNs for searching superflare events, we pursue an ideal vision that those automatically searched events are actually all and true positive superflare events in a database. At the present moment, the benefits of artificial intelligence are more reflected in efficiency while processing some repeatable jobs instead of handling extraordinary unseen situations. We still recommend readers who are willing to use our CNNs for searching superflare events to at least visually inspect the remaining not classified 8% data. And these data can also be used for enlarging superflare database for training six CNNs or other networks in the future.

5.3. Duration and amplitude

As we have discussed, superflare candidates with relative low SNR are hard to be visually inspected. The same also applies to those six CNNs trained before. It is possible that the duration and amplitude of a superflare can be related to the SNR of a superflare. These two properties can be intuitively recognized. Those superflares with long durations and large amplitudes are more obvious and have abundant superflare-features. In Figure 11, it is obvious that the performances of the stacking CNN is not better than the soft-voting, as shown in panels (a1), (a2), (b1) and (b2). The candidates with short durations and low peak amplitudes are not well classified than these with long durations and high amplitudes. In another words, the trained six CNNs or stacking CNN do not perform well on candidates with relative lower SNR. For soft-voting, greater performance is achieved by rejecting classification of candidates with shorter durations and lower peak amplitudes, as shown in panels (a3) and (b3) of Figure 11. So, when using classification results from CNNs in this work, we should pay more attention to those candidates which are classified as superflare events but with short durations and low peak amplitudes. In the future, the updates of six CNNs and stacking CNN in this work or constructed other CNNs should lay emphasis on superflare instances with lower SNRs. Here, we propose two ways, (1) collect more data with relative lower SNRs, and (2) make the time interval

of a superflare at the same scale of width for TD-arrays, PL-images and LS-images, through stretching or compressing the time axis.

6. SUMMARY

This work focuses on developing CNNs for superflare automatic searching on pixel-level data. We use 15,638 superflare candidates, which are classified into three categories, such as Gold-class, Silver-class and None-class. Examples of these classes are shown in Figure 2. These candidates are from 71,732 solar-type stars observed by three-years observation of *TESS*. These candidates are automatically searched through our previous methods (Tu et al. 2021, 2020), and visually inspected at least three times in this work. The information of solar-type stars and superflare properties are listed in Table 1 and Table 2.

Six CNNs have been trained and applied by k-folding cross validation. These six CNNs are trained by feature data including TD-arrays, PL-images and LS-images. All superflare candidates and feature data are public available. Examples of these feature data are visualized in Figure 3. As uneven counts of instances in Gold-class, Silver-class and None-class, data re-balancing is considered when training CNNs. These six CNNs are different from each other, which are developed with considering characteristics of different features.

Ensemble learning is used when combining all outputs of six CNNs. The trained six CNNs, stacking CNN and code are public available. After comparing indicators of networks' performance like accuracy, recall, precision, BEP and AUC of CNN, we found that the stacking and voting methods evidently enhance performance and generalization ability than six CNNs. The reason is that the combination of six CNNs depicts superflare features according to abundant points of view much more than a single CNN. The stacking CNN improves the redundancy or error-tolerant rate of searching superflares. Voting methods including soft-voting and hard-voting show better performance than stacking CNN, but the trade off classification rate reduces from 100% to about 92%. Meanwhile, the accuracy is improved from 97.62% to over 99%. Voting methods notice more on result consistency of six CNNs. We set a limit of 75% which ensures votes united from six CNNs are broadly representative, more accurate and reliable while searching superflares. Soft-voting is the best method, whose $R \sim 1$, $P \sim 1$, $FPR \sim 0$ and $TPR \sim 1$. 8% of unclassified data should be visually inspected one by one. These data is basically intractable with relatively low SNRs and hard to be classified. Visual inspection of these data will not only improve the accuracy to higher than 99.42%, but also enlarge the size of training database for six CNNs' updates in the future.

These six CNNs performance is better on superflare candidates with high SNRs (also with longer durations and higher peak amplitudes). Voting methods are more capable of rejecting those candidates with shorter durations and lower peak amplitudes. This is the reason why soft-voting is better than stacking CNN. The voting methods also give chances for finding new transient phenomena, as they are totally not recognized by trained CNNs at all, which will not be successively classified but left for visual inspection.

In this work, six CNNs and ensemble learning methods are developed for the purpose of automatically identify superflare events from pixel-level data, which ensures selected superflares are true positive events. Contamination of false positive events will influence the statistical analysis of superflare data. For instance, the number of non-superflares events is two times more than that of superflare events in the database of this work, whose statistical weight can not be neglected. Although superflare events in this work are selected from solar-type stars, the training CNNs are only based on observational data. Stellar parameters are not considered. So, these trained CNNs and methods can also be applied for detecting stellar flares on other types of stars. CNN training is time-costing and data-consuming. Performance and generalization of a CNN is also based on the scale of database. In the future, updating CNNs of this work should be still based on larger scale of superflare database, especially the superflares with low SNRs. CNNs will efficiently process archived and upcoming data from *TESS*. Namekata et al. (2021) probably found a stellar filament eruption associated with a superflare event through optical spectroscopic observation. If CNNs forecasting stellar superflare is available in the future, it will buy time for preparing follow up optical spectroscopic observation. And if so, the work by Wang et al. (2021) could also capture the whole spectroscopic observations from before to the end of the stellar flare, and Namekata et al. (2021) would not cost way too much precious ground observation time on to a single star. They would not probably find stellar filament eruption only by chance. Much more stellar CME events could be more efficiently detected. We can foresee that the scale of stellar superflare can be efficiently enlarged by CNNs in this work and more interesting statistical research could be done in the future, including but not limited to comparison of superflares on different types of stars.

ACKNOWLEDGEMENTS

We would like to thank B. B. Zhang, Niu Liu and Bo-yang Wang for valuable discussions and helps. We sincerely thank the Mikulski Archive for Space Telescopes (MAST) and the *TESS* community for applying reachable data portal and tools. This work is supported by the National Natural Science Foundation of China (grant No. U1831207) and the China Manned Space Project (CMS-CSST-2021-A12). The codes of this work were run on a high performance computing equipped with eight NVIDIA Tesla P100 GPU computing processors ¹.

Software: Jupyter Notebook (Kluyver et al. 2016), numpy (van der Walt et al. 2011), matplotlib (Hunter 2007), pandas (Wes McKinney 2010), lightkurve (Lightkurve Collaboration et al. 2018), astropy (Astropy Collaboration et al. 2013), astroquery (Ginsburg et al. 2019), pytorch (Paszke et al. 2019).

Facilities: TESS, Gaia, Hipparcos,

REFERENCES

- Agarwal, D., Aggarwal, K., Burke-Spolaor, S., Lorimer, D. R., & Garver-Daniels, N. 2020, MNRAS, 497, 1661, doi: [10.1093/mnras/staa1856](https://doi.org/10.1093/mnras/staa1856)
- Airapetian, V. S., Glocer, A., Gronoff, G., Hébrard, E., & Danchi, W. 2016, Nature Geoscience, 9, 452, doi: [10.1038/ngeo2719](https://doi.org/10.1038/ngeo2719)
- Astropy Collaboration, Robitaille, T. P., Tollerud, E. J., et al. 2013, A&A, 558, A33, doi: [10.1051/0004-6361/201322068](https://doi.org/10.1051/0004-6361/201322068)
- Atri, D. 2017, MNRAS, 465, L34, doi: [10.1093/mnras/slw199](https://doi.org/10.1093/mnras/slw199)
- Basri, G., Walkowicz, L. M., Batalha, N., et al. 2010, ApJL, 713, L155, doi: [10.1088/2041-8205/713/2/L155](https://doi.org/10.1088/2041-8205/713/2/L155)
- Bishop, C. M. 2006, Pattern Recognition and Machine Learning (Information Science and Statistics) (Berlin, Heidelberg: Springer-Verlag)
- Breiman, L. 1996, Machine learning, 24, 49
- Chen, B. H., Hashimoto, T., Goto, T., et al. 2022, MNRAS, 509, 1227, doi: [10.1093/mnras/stab2994](https://doi.org/10.1093/mnras/stab2994)
- Cui, K., Liu, J., Feng, F., & Liu, J. 2022, AJ, 163, 23, doi: [10.3847/1538-3881/ac3482](https://doi.org/10.3847/1538-3881/ac3482)
- Cui, K., Liu, J., Yang, S., et al. 2019, MNRAS, 489, 5513, doi: [10.1093/mnras/stz2432](https://doi.org/10.1093/mnras/stz2432)
- Doyle, L., Ramsay, G., & Doyle, J. G. 2020, MNRAS, 494, 3596, doi: [10.1093/mnras/staa923](https://doi.org/10.1093/mnras/staa923)
- Duchi, J., Hazan, E., & Singer, Y. 2011, Journal of Machine Learning Research, 12, 2121
- Feinstein, A. D., Montet, B. T., Ansdell, M., et al. 2020, AJ, 160, 219, doi: [10.3847/1538-3881/abac0a](https://doi.org/10.3847/1538-3881/abac0a)
- Feinstein, A. D., Seligman, D. Z., Günther, M. N., & Adams, F. C. 2021, arXiv e-prints, arXiv:2109.07011. <https://arxiv.org/abs/2109.07011>
- Gaia Collaboration, Brown, A. G. A., Vallenari, A., et al. 2020, arXiv e-prints, arXiv:2012.01533. <https://arxiv.org/abs/2012.01533>
- . 2018, A&A, 616, A1, doi: [10.1051/0004-6361/201833051](https://doi.org/10.1051/0004-6361/201833051)
- Georgoulis, M. K., Bloomfield, D. S., Piana, M., et al. 2021, Journal of Space Weather and Space Climate, 11, 39, doi: [10.1051/swsc/2021023](https://doi.org/10.1051/swsc/2021023)
- Ginsburg, A., Sipőcz, B. M., Brasseur, C. E., et al. 2019, AJ, 157, 98, doi: [10.3847/1538-3881/aafc33](https://doi.org/10.3847/1538-3881/aafc33)
- He, H., Wang, H., Zhang, M., et al. 2018, ApJS, 236, 7, doi: [10.3847/1538-4365/aab779](https://doi.org/10.3847/1538-4365/aab779)
- He, Z., Er, X., Long, Q., et al. 2020, MNRAS, 497, 556, doi: [10.1093/mnras/staa1917](https://doi.org/10.1093/mnras/staa1917)
- Hudson, H. S. 2021, ARA&A, 59, doi: [10.1146/annurev-astro-112420-023324](https://doi.org/10.1146/annurev-astro-112420-023324)
- Hunter, J. D. 2007, Computing in Science and Engineering, 9, 90, doi: [10.1109/MCSE.2007.55](https://doi.org/10.1109/MCSE.2007.55)
- Ip, W.-H., Kopp, A., & Hu, J.-H. 2004, ApJL, 602, L53, doi: [10.1086/382274](https://doi.org/10.1086/382274)
- Kluyver, T., Ragan-Kelley, B., Pérez, F., et al. 2016, in Positioning and Power in Academic Publishing: Players, Agents and Agendas, ed. F. Loizides & B. Schmidt, IOS Press, 87 – 90
- Kussul, E., & Baidyk, T. 2004, Image and Vision Computing, 22, 971, doi: <https://doi.org/10.1016/j.imavis.2004.03.008>
- Lecun, Y., Bottou, L., Bengio, Y., & Haffner, P. 1998, Proceedings of the IEEE, 86, 2278, doi: [10.1109/5.726791](https://doi.org/10.1109/5.726791)
- Lightkurve Collaboration, Cardoso, J. V. d. M., Hedges, C., et al. 2018, Lightkurve: Kepler and TESS time series analysis in Python, Astrophysics Source Code Library. <http://ascl.net/1812.013>
- Lingam, M., & Loeb, A. 2017, ApJ, 848, 41, doi: [10.3847/1538-4357/aa8e96](https://doi.org/10.3847/1538-4357/aa8e96)
- Lomb, N. R. 1976, Ap&SS, 39, 447, doi: [10.1007/BF00648343](https://doi.org/10.1007/BF00648343)
- Maehara, H., Shibayama, T., Notsu, Y., et al. 2015, Earth, Planets, and Space, 67, 59, doi: [10.1186/s40623-015-0217-z](https://doi.org/10.1186/s40623-015-0217-z)

¹ <https://www.nvidia.com/en-sg/data-center/tesla-p100/>

- Maehara, H., Shibayama, T., Notsu, S., et al. 2012, *Nature*, 485, 478, doi: [10.1038/nature11063](https://doi.org/10.1038/nature11063)
- Namekata, K., Maehara, H., Honda, S., et al. 2021, *Nature Astronomy*, doi: [10.1038/s41550-021-01532-8](https://doi.org/10.1038/s41550-021-01532-8)
- Notsu, Y., Maehara, H., Honda, S., et al. 2019, *ApJ*, 876, 58, doi: [10.3847/1538-4357/ab14e6](https://doi.org/10.3847/1538-4357/ab14e6)
- Ofman, L., Averbuch, A., Shlisselberg, A., et al. 2022, *NewA*, 91, 101693, doi: [10.1016/j.newast.2021.101693](https://doi.org/10.1016/j.newast.2021.101693)
- Paszke, A., Gross, S., Massa, F., et al. 2019, in *Advances in Neural Information Processing Systems 32*, ed. H. Wallach, H. Larochelle, A. Beygelzimer, F. d'Alché-Buc, E. Fox, & R. Garnett (Curran Associates, Inc.), 8024–8035
- Rao, S., Mahabal, A., Rao, N., & Raghavendra, C. 2021, *MNRAS*, 502, 2845, doi: [10.1093/mnras/stab203](https://doi.org/10.1093/mnras/stab203)
- Rubenstein, E. P., & Schaefer, B. E. 2000, *ApJ*, 529, 1031, doi: [10.1086/308326](https://doi.org/10.1086/308326)
- Scargle, J. D. 1982, *ApJ*, 263, 835, doi: [10.1086/160554](https://doi.org/10.1086/160554)
- Segura, A., Walkowicz, L. M., Meadows, V., Kasting, J., & Hawley, S. 2010, *Astrobiology*, 10, 751, doi: [10.1089/ast.2009.0376](https://doi.org/10.1089/ast.2009.0376)
- Shibata, K., Isobe, H., Hillier, A., et al. 2013, *PASJ*, 65, 49, doi: [10.1093/pasj/65.3.49](https://doi.org/10.1093/pasj/65.3.49)
- Shibayama, T., Maehara, H., Notsu, S., et al. 2013, *ApJS*, 209, 5, doi: [10.1088/0067-0049/209/1/5](https://doi.org/10.1088/0067-0049/209/1/5)
- Stassun, K. G., Oelkers, R. J., Paegert, M., et al. 2019, *AJ*, 158, 138, doi: [10.3847/1538-3881/ab3467](https://doi.org/10.3847/1538-3881/ab3467)
- Tu, Z.-L., Yang, M., Wang, H. F., & Wang, F. Y. 2021, *ApJS*, 253, 35, doi: [10.3847/1538-4365/abda3c](https://doi.org/10.3847/1538-4365/abda3c)
- Tu, Z.-L., Yang, M., Zhang, Z. J., & Wang, F. Y. 2020, *ApJ*, 890, 46, doi: [10.3847/1538-4357/ab6606](https://doi.org/10.3847/1538-4357/ab6606)
- van der Walt, S., Colbert, S. C., & Varoquaux, G. 2011, *Computing in Science and Engineering*, 13, 22, doi: [10.1109/MCSE.2011.37](https://doi.org/10.1109/MCSE.2011.37)
- van Leeuwen, F. 2007, *A&A*, 474, 653, doi: [10.1051/0004-6361:20078357](https://doi.org/10.1051/0004-6361:20078357)
- Vida, K., Bódi, A., Szklenár, T., & Seli, B. 2021, *A&A*, 652, A107, doi: [10.1051/0004-6361/202141068](https://doi.org/10.1051/0004-6361/202141068)
- Vida, K., & Roettenbacher, R. M. 2018, *A&A*, 616, A163, doi: [10.1051/0004-6361/201833194](https://doi.org/10.1051/0004-6361/201833194)
- Walkowicz, L. M., Basri, G., Batalha, N., et al. 2011, *AJ*, 141, 50, doi: [10.1088/0004-6256/141/2/50](https://doi.org/10.1088/0004-6256/141/2/50)
- Wang, J., Xin, L. P., Li, H. L., et al. 2021, *ApJ*, 916, 92, doi: [10.3847/1538-4357/ac096f](https://doi.org/10.3847/1538-4357/ac096f)
- Wes McKinney. 2010, in *Proceedings of the 9th Python in Science Conference*, ed. Stéfan van der Walt & Jarrod Millman, 56 – 61, doi: [10.25080/Majora-92bf1922-00a](https://doi.org/10.25080/Majora-92bf1922-00a)
- Wolpert, D. H. 1992, *Neural Networks*, 5, 241, doi: [https://doi.org/10.1016/S0893-6080\(05\)80023-1](https://doi.org/10.1016/S0893-6080(05)80023-1)
- Wu, C.-J., Ip, W.-H., & Huang, L.-C. 2015, *ApJ*, 798, 92, doi: [10.1088/0004-637X/798/2/92](https://doi.org/10.1088/0004-637X/798/2/92)
- Xiao, H., Rasul, K., & Vollgraf, R. 2017, arXiv e-prints, arXiv:1708.07747. <https://arxiv.org/abs/1708.07747>
- Yang, H., & Liu, J. 2019, *ApJS*, 241, 29, doi: [10.3847/1538-4365/ab0d28](https://doi.org/10.3847/1538-4365/ab0d28)
- Yang, X., Zhang, S. B., Wang, J. S., et al. 2021, *MNRAS*, 507, 3238, doi: [10.1093/mnras/stab2275](https://doi.org/10.1093/mnras/stab2275)
- Zhang, Y., Zhao, Y., & Wu, X.-B. 2021, *MNRAS*, 503, 5263, doi: [10.1093/mnras/stab744](https://doi.org/10.1093/mnras/stab744)
- Zhou, Z. 2021, *Machine Learning* (Springer), doi: [10.1007/978-981-15-1967-3](https://doi.org/10.1007/978-981-15-1967-3)

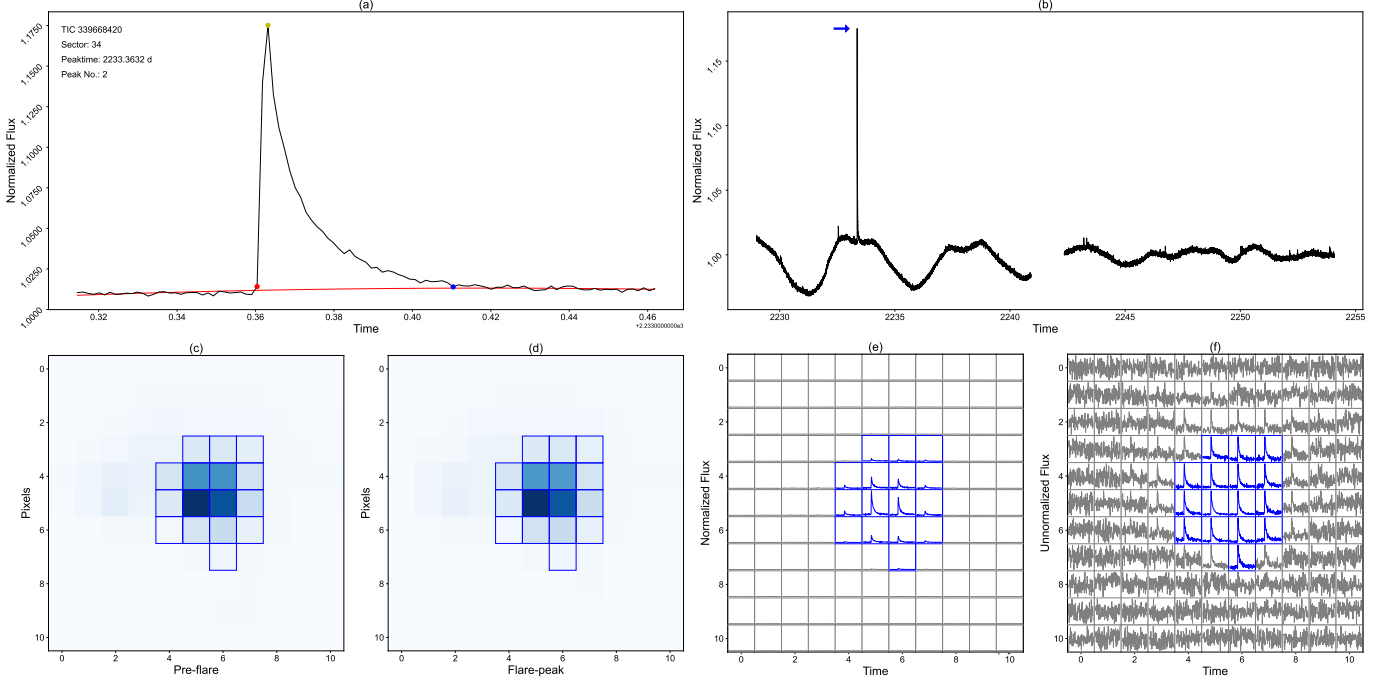
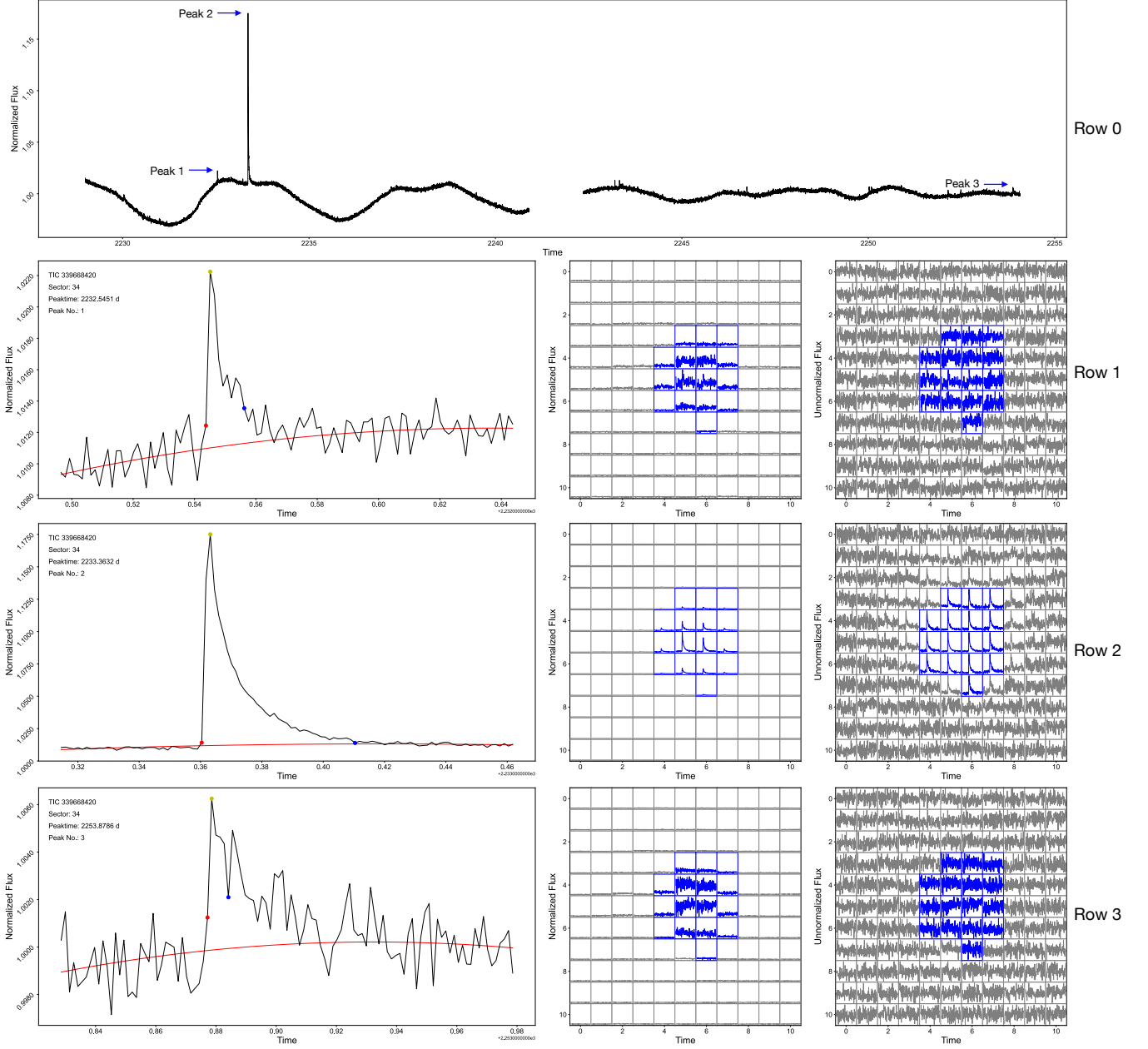


Figure 1. Patterns for visually inspecting superflares. The light curve of a superflare candidate is shown in panel (a). Here, $F(t)$ in Equation 4 is represented by the black solid line. $F_q(t)$ is shown by the red solid line. Yellow, red and blue dot circles represent the peak, start, and end time stamps of this superflare, respectively. The panel (b) gives the whole light curve of the sector, from which this superflare candidate is searched. And the peak of this superflare is pointed by the blue arrow mark. Panels (c) and (d) show the pixel-level images at the pre-flare and peak time stamps of the superflare, respectively. For each pixel in the images, its light curves with normalized and un-normalized flux are correspondingly shown in the square frames of the panel (e) and (f). Aperture masks by *TESS* pipeline are shown by blue frames in these lower panels.



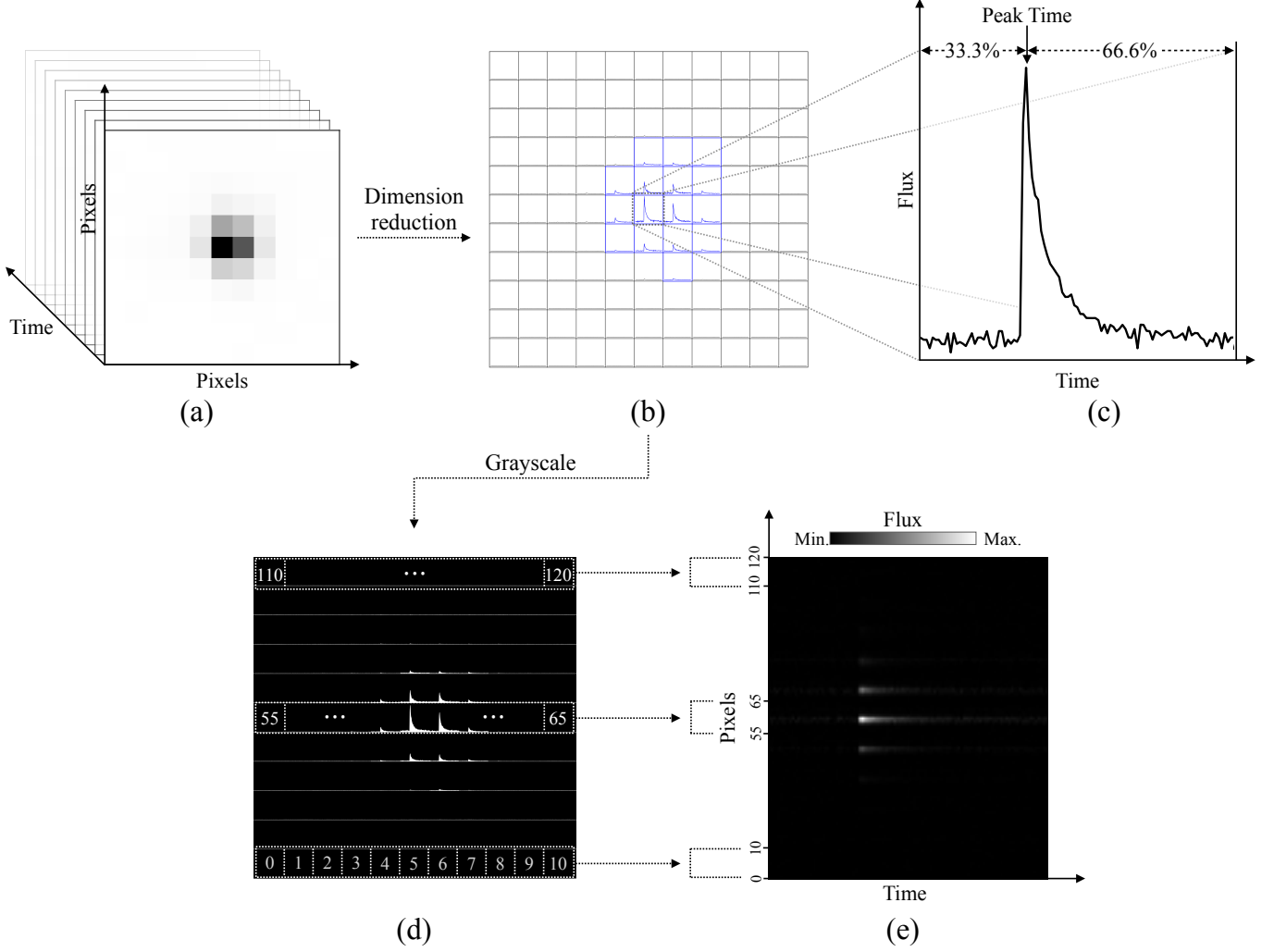
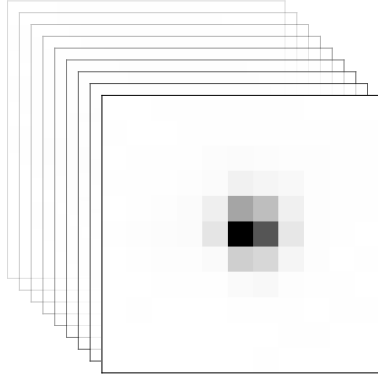
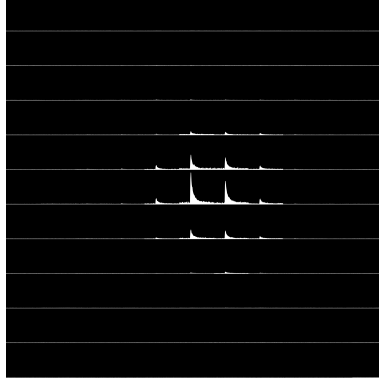


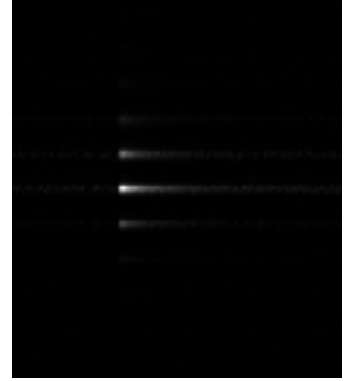
Figure 3. (a) Visualization of three dimension array of pixel-level data. The data covers the whole flare time interval from 0.05 days before to 0.10 days after the flare peak. All time stamps from original *TESS* data are kept. Each time-slice represents the pixel-level image at a specific time stamp. (b) Dimension reduction of the data in panel (a). We derive the light curve of each pixel in the image and reveal the light curve in the square. The square corresponds to the exact pixel site in pixel-level image. This panel is exactly same as the panel (e) and (f) of Figure 1 with normalized flux. (c) Zoom in one pixel light curve in panel (b). The x-axis and y-axis represent time and flux, respectively. The peak of a candidate is set at the 33.3% (1/3) position of the whole light curve. (d) Convert pixel level light curves to the image with grayscale color. Blue frames in panel (b) represent the masked apertures by *TESS*, in which light curves are correspondingly colored in white in panel (d). Other light curves are colored in grey. Area under the light curves are filled, which is for protruding the pinnacle-shape of superflare light curve. This is an example image of PL-normalized. (e) An example image of LS-normalized. We label all pixel light curves from left to right and from bottom to top as channel 0 to 120 in panel (d). Light curves displayed in each channel can be treated as an one-dimension array, of which each value represents flux and index sequences represent time series. In panel (e), we transform the way to display these data by lining up all sequences of channels from 0 to 120 as y-axis. The x-axis represents time series. And flux is presented by brightness of grayscale color. So, each horizontal line of this image stands for an array data displayed as pixel light curve in the corresponding frame of the image shown in panel (d). Pixel light curves with un-normalize flux (the panel (f) of Figure 1) are also transformed through above procedures. Examples of PL-unnormalized and LS-unnormalized can be found in Figure 4.



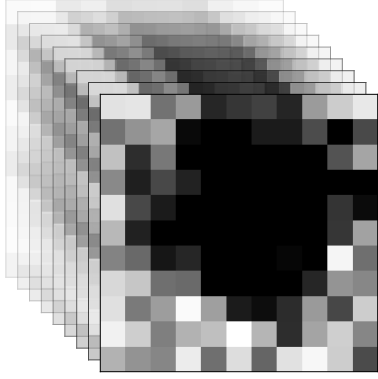
Three-dimension data
with normalized flux
(TD-normal.)



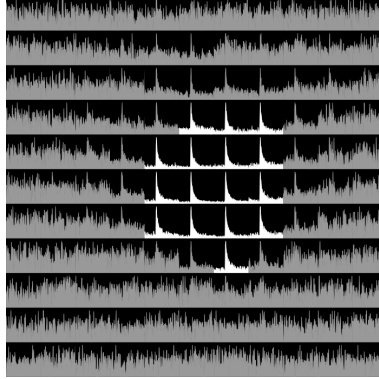
Pixel-level light curves
with normalized flux
(PL-normal.)



Line-up sequences of light
curves with normalized flux
(LS-normal.)



Three-dimension data
with unnormalized flux
(TD-unnormal.)



Pixel-level light curves
with un-normalized flux
(PL-unnormal.)



Line-up sequences of light
curves with un-normalized flux
(LS-unnormal.)

Figure 4. Examples of TD-arrays, PL-images, and LS-images, which are all derived from the candidate displayed in Figure 1. Here, normal. and unnormal. represent whether flux data are normalized and unnormalized. Figure 3 illustrates how we get these feature images. Examples of TD-normal. and TD-unnormal. may not be accurately visualized. However, these two kinds of data are three-dimension arrays with one dimension which is for describing time. These arrays can be understood as film clips, which reveal changing of pixel-level image during the whole flare times. In PL-normal. and PL-unnormal. images, flare light curves which are colored in white are those data from apertures masked by *TESS*. Other pixel light curves are colored in grey.

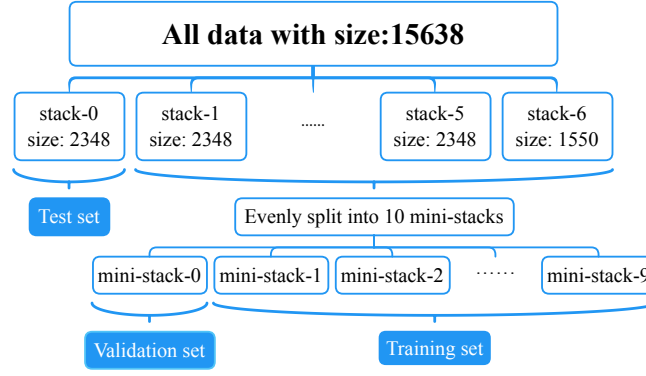


Figure 5. Flow chart for setting the training, validation and test data sets. As shown by this work flow, we have seven test data sets, each of them corresponds to ten validation and ten training sets. Data balance between three classes are considered when we split data into stacks and mini-stacks. Training set, validation set and test set take 75%, 10%, and 15% of the whole database. Separating into stacks and mini-stacks is for k-folding cross validation.

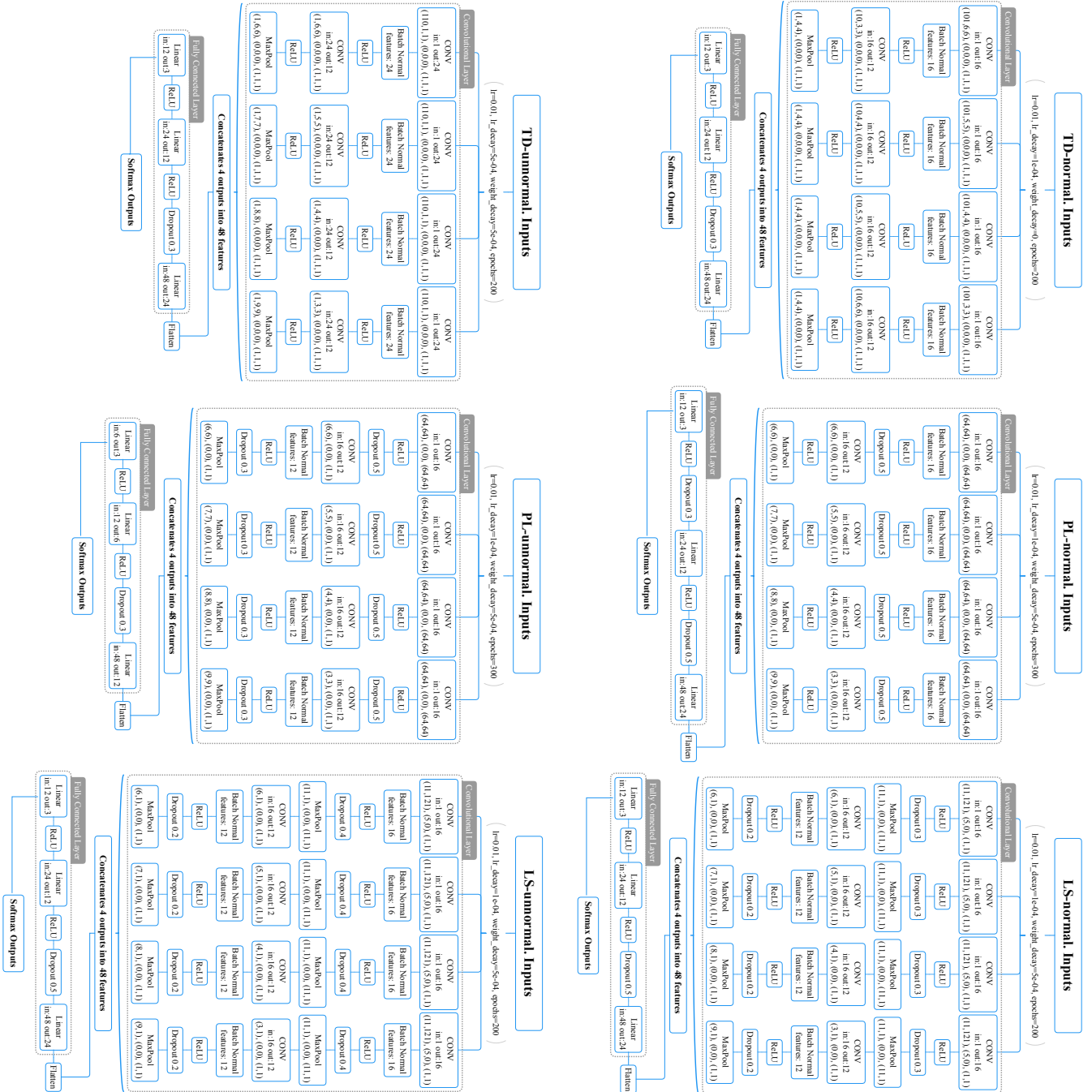


Figure 6. Flow charts of six convolutional neural networks. For each network, its learning rate (lr), learning rate decay (lr_decay), weight decay and epochs are all listed under the title of network. All networks are constructed by convolutional layer and fully connected layer. Three brackets in some layers mean neural kernel size, kernel moving stride, and padding size, respectively. The numbers of input-channels and output-channels are also listed in the layer. The outputs of each network are applied to Softmax function (Equation 7), so outputs can be regarded as probabilities for classifying a candidate into three classes.

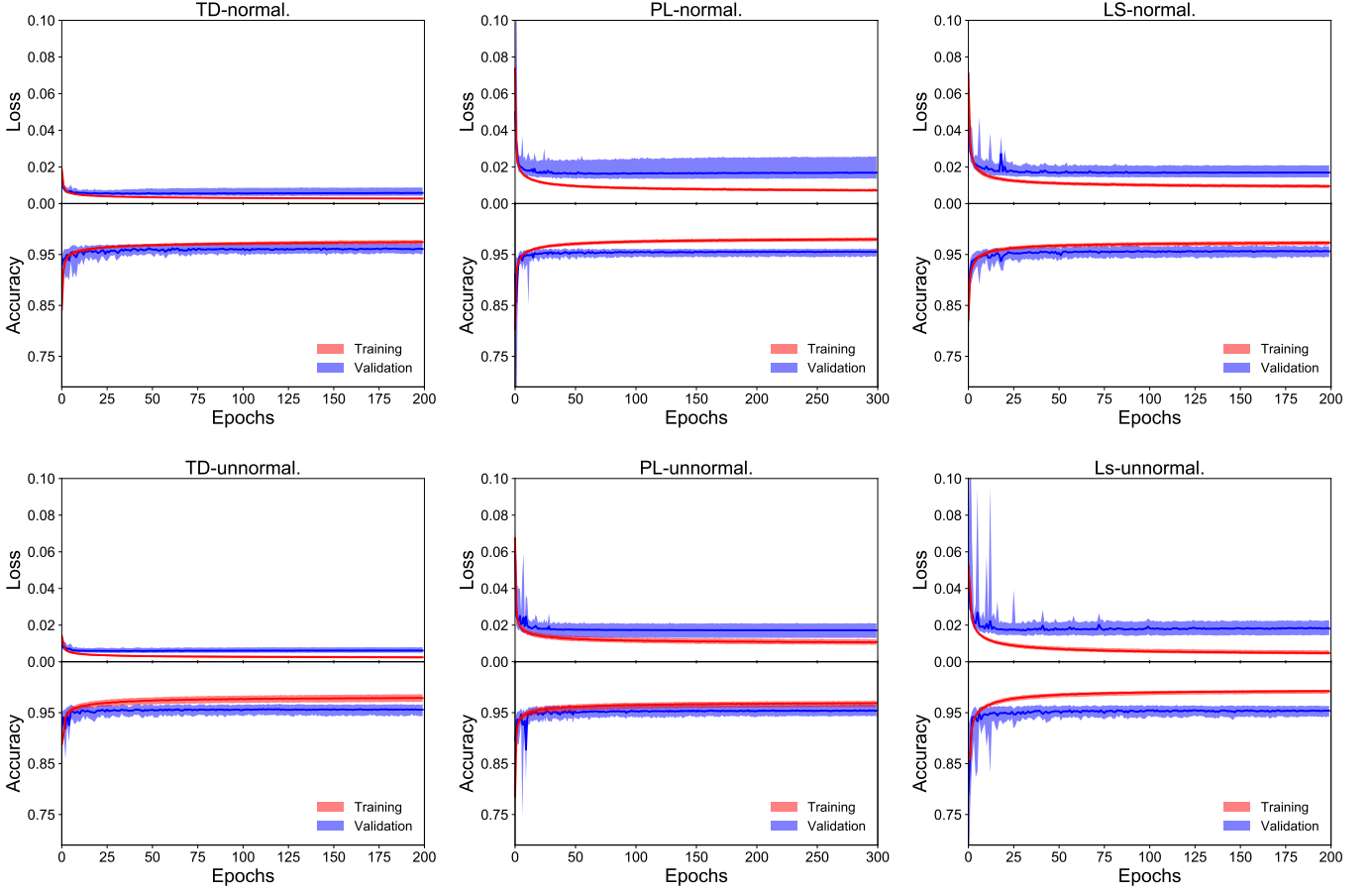


Figure 7. The loss and accuracy vs. training epochs for six CNNs. The outputs of each network give the probabilities of classifying into three classes. Gold-class and Silver-class both stand for superflare events. The accuracy represents the right-classification rate of superflare and non-superflare events. In another words, even if outputs give three probabilities, we only distinguish superflare and non-superflare events. Results are from 70 training and validation data sets. Blue and red represent results of validation and training set as training epochs increasing. Solid colored lines stand for the median values of results from all data sets. Shaded area stands for 5% to 95% of each result.

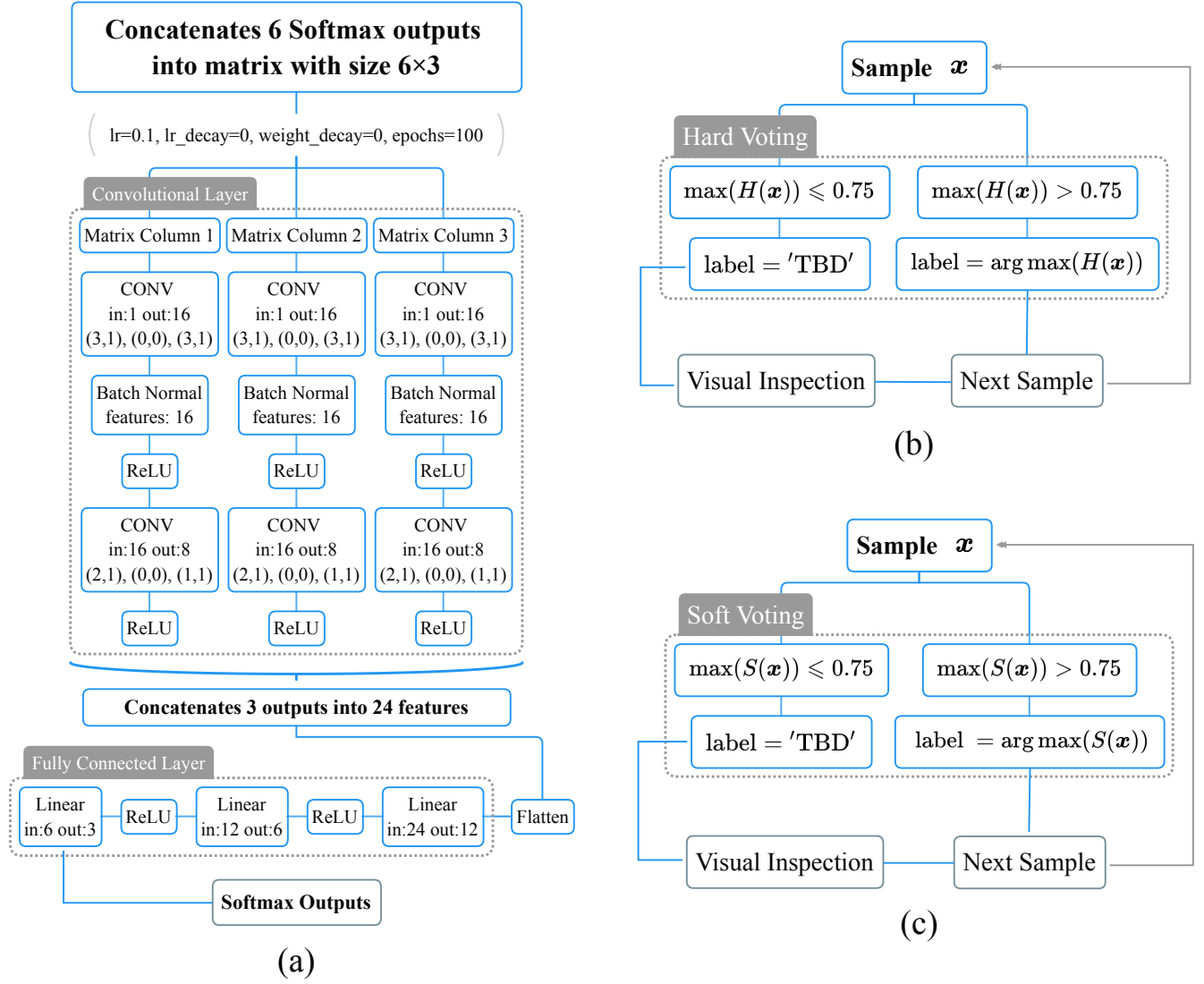


Figure 8. Work flows of stacking CNN, hard-voting and soft-voting are shown in panel (a), (b) and (c), respectively. Inputs of stacking CNN are arrays with size 6x3 and values coming from combined outputs of six CNNs shown in Figure 6. In voting flows, label = 'TBD' means classification of the candidate is to be determined after visual inspection.

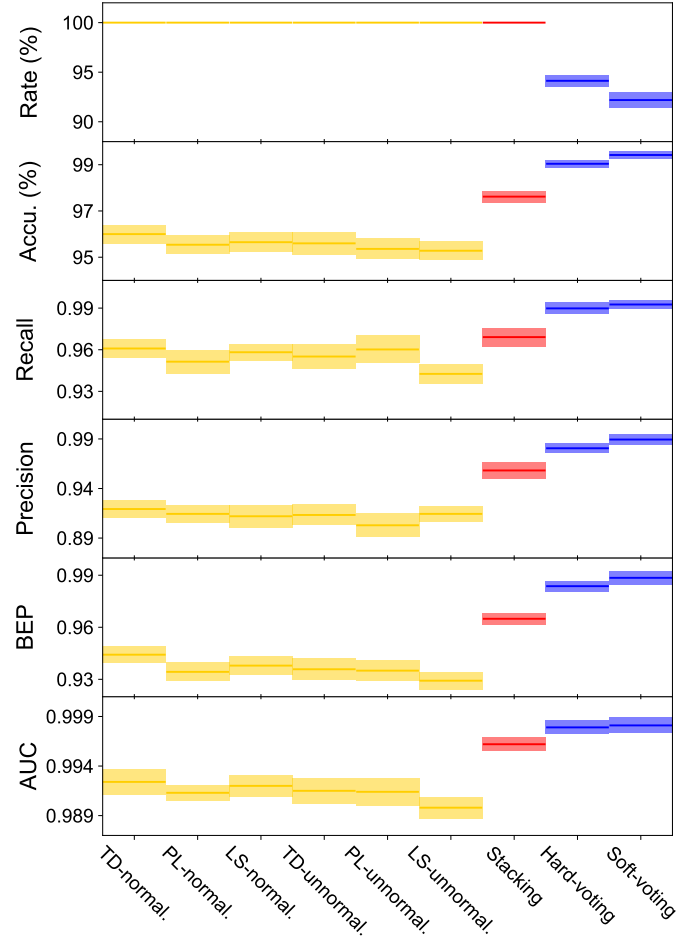


Figure 9. Visualization of properties in Table 3. Solid lines and shaded area show mean values and standard deviations of each property. Yellow, red and blue stand for six CNNs, stacking CNN, and voting methods, respectively.

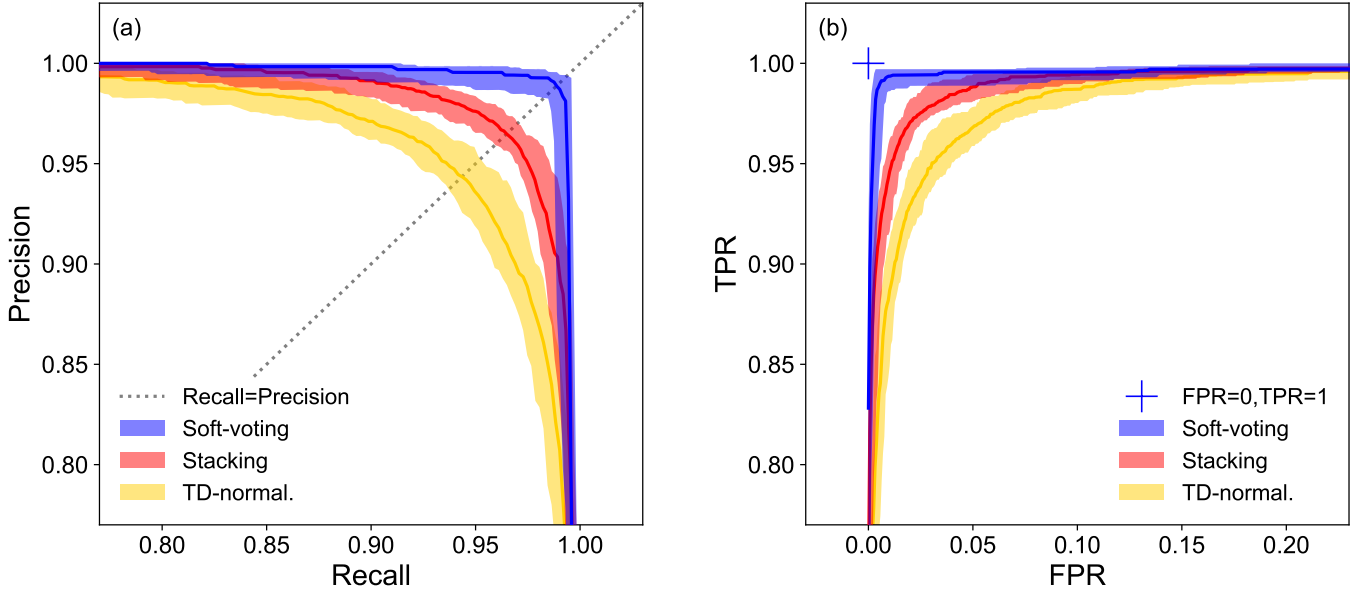


Figure 10. PR-curve and ROC-curve are shown in panels (a) and (b). Dashed grey line in panel (a) represents Recall = Precision. Blue cross mark in panel (b) represents the point, where $FPR = 0$, $TPR = 1$. This is the result from the best ideal network, as all positive candidates are selected without any negative ones. As TD-normal. is the best network of six CNNs and soft-voting is better than hard-voting method, we use the results from these two to comparing with stacking CNN. Results from soft-voting, stacking CNN and TD-normal. are shown in blue, red and yellow. Solid curves represent the median values of results. Shaded area stand for ranges of each property from 5% to 95%.

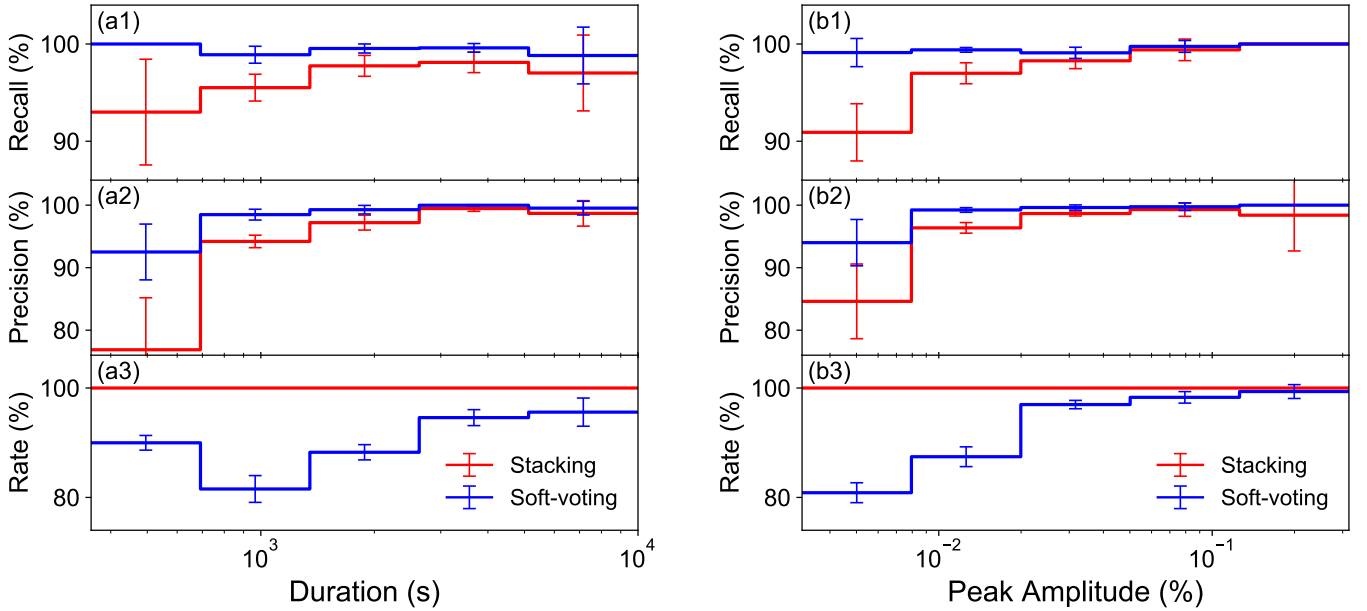


Figure 11. Specific recall, precision and classification rate in each bin of superflare duration and amplitude. Bin size of duration and amplitude is in log scale. We compare stacking CNN with soft-voting, and represented by red and blue curves, respectively. Recall and precision are defined in Equations (11) and (12). Rate stands for classification rate as we defined in Equation (18). These three properties are all in unit of percentile in this figure. Error bars are standard deviations of each properties. Data from which we get this figure is the same with those of Figure 9, Figure 10 and Table 3, but with specific results from bins of duration and peak amplitude.

Table 1. Properties of solar-type stars.

<i>TESS</i> ID	T_{mag}^a	T_{eff}^b (K)	$\log g^c$	Radius ^d (R_{\odot})	Period ^e ($days$)	Rvar ^f	Flag ^g
260268381	9.22	5894	4.00	1.71	5.73	0.002219	...
152937588	9.12	5660	4.12	1.46	3.49	0.002008	...
410214986	7.85	5414	4.45	0.95	3.58	0.056958	HB
260188537	9.31	5540	4.02	1.59	7.48	0.008919	GB21
197959959	9.37	5353	4.36	1.05	6.97	0.005462	GB42
261463150	10.15	5838	4.58	0.87	9.29	0.003536	GM21
141425702	10.99	5718	4.52	0.92	13.42	0.006033	GM42

NOTE.

^a *TESS* magnitude.^b Surface effective temperature of the star in unit of K .^c Surface gravity of the star in log scale.^d Stellar radius in unit of R_{\odot} .The above properties are all from *TESS* input catalogue (TIC v8) (Stassun et al. 2019).^e Periodicity of the star in unit of days.^f Stellar photometric variability (R_{var}) as defined in Equation 1.^g Flags for stars after cross-matching with catalogs from *Hipparcos-2* and *Gaia*-EDR3. Here, HB stands for stars may be binary systems from *Hipparcos-2* catalog. GM and GB stand for the stars may contain M-dwarfs or other brighter stars nearby, which are collected by *Gaia*-EDR3. 21 and 42 stand for the possible contamination, which are located within 21'' or within 21'' to 42'' distance from the main targets.

(All data in this table is available in machine-readable form.)

Table 2. Information of superflare candidates

<i>TESS</i> ID	Sector ^a	Source ^b	Peak No. ^c	Label ^d	Peak Date ^e	Peak Lumi. ^f (erg s ⁻¹)	Energy ^g (erg)	Duration ^h (s)	File name ⁱ
Gold-class counts: 1,268									
382575967	7	long	Peak11	0	1512.1703	1.68E+32	4.74E+35	6840.11	1s_long_normalize-TIC382575967_Q7_Peak11.png...
55752857	22	short	Peak0	0	1923.5225	4.39E+32	1.07E+36	5999.85	1s_short_normalize-TIC55752857_Q22_Peak0.png...
260268898	31	short	Peak0	0	2163.4045	7.32E+31	7.05E+34	1920.03	1s_short_normalize-TIC260268898_Q31_Peak0.png...
260268898	32	short	Peak0	0	2177.9102	5.17E+31	8.02E+34	2880.04	1s_short_normalize-TIC260268898_Q32_Peak0.png...
260268898	35	short	Peak1	0	2278.9417	7.55E+31	9.97E+34	4079.91	1s_short_normalize-TIC260268898_Q35_Peak1.png...
.....									
Silver-class counts: 3,792									
339668420	30	short	Peak5	1	2135.0738	3.29E+31	3.54E+34	2040.04	1s_short_normalize-TIC339668420_Q30_Peak5.png...
235930066	24	long	Peak1	1	1958.7945	1.45E+31	7.60E+33	839.99	1s_long_normalize-TIC235930066_Q24_Peak1.png...
294098955	6	short	Peak0	1	1476.7159	4.57E+31	2.62E+34	840.01	1s_short_normalize-TIC294098955_Q6_Peak0.png...
339668420	34	long	Peak0	1	2230.0340	1.50E+31	2.80E+34	2640.04	1s_long_normalize-TIC339668420_Q34_Peak0.png...
140891597	28	short	Peak0	1	2064.9989	7.57E+31	1.65E+35	3479.99	1s_short_normalize-TIC140891597_Q28_Peak0.png...
.....									
None-class counts: 10,578									
36828969	4	short	Peak2	2	1423.4314	-	-	-	1s_short_normalize-TIC36828969_Q4_Peak2.png...
1119096	4	short	Peak0	2	1423.2551	-	-	-	1s_short_normalize-TIC1119096_Q4_Peak0.png...
1119096	4	short	Peak1	2	1423.2912	-	-	-	1s_short_normalize-TIC1119096_Q4_Peak1.png...
406413428	31	short	Peak2	2	2161.8467	-	-	-	1s_short_normalize-TIC406413428_Q31_Peak2.png...
363225381	39	short	Peak0	2	2381.7991	-	-	-	1s_short_normalize-TIC363225381_Q39_Peak0.png...
.....									

NOTE.

^a Sector No. of *TESS*, in which superflare candidates are captured

^b 'long' and 'short' stand for $n = 5$ and $n = 2$ in Equation 2.

^c The serial number of a flare candidate captured from the star in a specific sector. For example, the first row stand for the candidate, which is the eleventh one detected from the light curve of TIC382575967 in sector seven, and $n = 5$ is set in Equation 2.

^d Labels of Gold-class, Silver-class and None-class, which is represented by 0, 1, and 2, respectively. All labels are set by visual inspection of candidates. Here, we have 1,268 candidates in Gold-class, 3,792 candidates in Silver-class. And other 10,578 candidates are in None-class.

^e Superflare peak timestamps of *TESS*.

^f Superflare peak luminosity in unit of $erg\ s^{-1}$.

^g Superflare energy in unit of erg , which is calculated by the Equation 6.

^h Superflare duration in unit of s , which is calculated by $t_{end} - t_{start}$. Start and end times of superflare is derived through Equation 5.

ⁱ File name of feature images and arrays of the candidate. These files are used for training CNNs. Their names are structured by types of data, the number of sector, source, and the serial number of the candidate. Note that, data of TD-normal. and TD-unnormal. are not saved in any picture formats but in array format of *Numpy* (a *Python* package) with filename extension *.npy*.

(All data in this table is available in machine-readable form.)

Table 3. Results of CNNs

	Network	Class. Rate (%)	Accuracy (%)	Recall	Precision	BEP	AUC
Six CNNs	TD-normal.	100	96.00 ± 0.41	0.9609 ± 0.0066	0.9193 ± 0.0090	0.9442 ± 0.0048	0.9924 ± 0.0013
	PL-normal.	100	95.54 ± 0.40	0.9514 ± 0.0085	0.9144 ± 0.0089	0.9343 ± 0.0052	0.9913 ± 0.0008
	LS-normal.	100	95.65 ± 0.43	0.9582 ± 0.0061	0.9120 ± 0.0116	0.9379 ± 0.0052	0.9920 ± 0.0011
	TD-unnormal.	100	95.60 ± 0.48	0.9551 ± 0.0088	0.9133 ± 0.0104	0.9358 ± 0.0062	0.9915 ± 0.0013
	PL-unnormal.	100	95.36 ± 0.45	0.9602 ± 0.0098	0.9029 ± 0.0118	0.9350 ± 0.0058	0.9914 ± 0.0014
	LS-unnormal.	100	95.28 ± 0.39	0.9426 ± 0.0072	0.9144 ± 0.0079	0.9292 ± 0.0050	0.9898 ± 0.0011
Ensemble Learning	Stacking	100	97.62 ± 0.25	0.9691 ± 0.0068	0.9582 ± 0.0083	0.9649 ± 0.0033	0.9962 ± 0.0007
	Hard Voting	94.13 ± 0.58	99.04 ± 0.16	0.9898 ± 0.0043	0.9806 ± 0.0047	0.9842 ± 0.0026	0.9927 ± 0.0020
	Soft Voting	92.19 ± 0.77	99.42 ± 0.16	0.9926 ± 0.0032	0.9894 ± 0.0052	0.9885 ± 0.0039	0.9981 ± 0.0008

NOTE.

Class. Rate is classification rate defined in Equation 18. Accuracy, recall, and precision are defined in Equations (10), (11), and (12), respectively. BEP and AUC are introduced in Section 3.3. Mean and standard deviations of each property are listed in the table.